ADVANCED MATERIALS INTERFACES
www.advmatinterfaces.de

Fe/Sb_2Te_3 Interface Reconstruction through Mild Thermal Annealing

Emanuele Longo, Claudia Wiemer, Raimondo Cecchini, Massimo Longo, Alessio Lamperti, Anton Khanas, Andrei Zenkevich, Matteo Cantoni, Christian Rinaldi, Marco Fanciulli, and Roberto Mantovan**

When coupled with ferromagnetic layers (FM), topological insulators (TI) are expected to boost the charge-to-spin conversion efficiency across the FM/TI interface. In this context, a thorough control and optimization of the FM/TI interface quality are requested. Here, the evolution of the chemical, structural, and magnetic properties of the Fe/Sb_2Te_3 heterostructure is presented as a function of a rapid mild thermal annealing conducted on the Sb_2Te_3-TI (up to 200 °C). While the bilayer is not subjected to any thermal treatment upon Fe deposition, the annealing of Sb_2Te_3 markedly improves its crystalline quality, leading to an increase in the fraction of ferromagnetic Fe atoms at the buried Fe/Sb_2Te_3 interface and a slight lowering of the magnetic coercivity of the Fe layer. The method is an efficient tool to clean up the Fe/Sb_2Te_3 interface, which may be extended to different FM/TI heterostructures. Simultaneously to the interface reconstruction, a constant ≈20% fraction of FeTe develops at the interface. Since FeTe can display superconductivity, the Fe/Sb_2Te_3 system could have potentialities for exploiting phenomena at the edge of magnetism, superconductivity and topology.

1. Introduction

Topological insulators (TI) are gaining attention in the context of spintronics as ideal candidates for the replacement of heavy metals (Pt, Ta, etc.) at the interface with ferromagnetic layers (FM) in systems exploiting spin-to-charge conversion effects.[1–4]

However, there are several aspects to investigate. First, the role played by the specific chemical bonds and/or the presence of magnetically dead layers in affecting the spin-to-charge conversion efficiency is not completely understood. So, an investigation and optimization of the chemical, structural and magnetic properties of the FM/TI interfaces[2,5] is mandatory. Moreover, from the technological point of view, the growth of FM is usually conducted ex situ, after the synthesis of TI. The surface of the TI is often protected by a capping layer during the transfer,[6] but the efficient removal of such protective layer is not always easy, and the trade-off between benefits and criticalities in using an interlayer, is still under debate.

We propose an alternative method to prepare the TI surface, consisting of a mild rapid thermal annealing (RTA) process prior to the FM deposition. In particular, our focus is the interface between Fe and the 3D-TI Sb_2Te_3 produced by metal–organic chemical vapor deposition (MOCVD).[7] A previous study of as-deposited Fe/Sb_2Te_3 heterostructures[8] revealed that only 50% of the Fe atoms at the interface (out of the 1 nm Fe in contact with Sb_2Te_3) were coordinated in a pure ferromagnetic phase. The remaining part of the Fe atoms at the interface were found in paramagnetic configurations, detrimental in view of charge-to-spin interconversion. As compared to results available for similar systems,[9–12] a general bonding mechanism was suggested, involving the Fe atoms and the chalcogenide element in chalcogenide-based TI.

Here, we demonstrate that the proposed RTA methodology improves the TI structural quality and promotes the Fe/Sb_2Te_3 interface reconstruction, yielding the maximization of the ferromagnetic component in contact with the TI. To this aim, we combined interface-sensitive ^{57}Fe conversion electron Mössbauer spectroscopy (CEMS), grazing incidence X-ray diffraction and reflectivity (GIXRD/XRR), time-of-flight secondary ions mass spectrometry (ToF-SIMS) and vibrating sample magnetometry (VSM). The proposed method can be easily extended

E. Longo, Dr. C. Wiemer, Dr. R. Cecchini, Dr. M. Longo, Dr. A. Lamperti, Dr. R. Mantovan
CNR-IMM
Unit of Agrate Brianza
Via C. Olivetti 2, Agrate Brianza 20864, Italy
E-mail: emanuele.longo@mdm.imm.cnr.it; roberto.mantovan@mdm.imm.cnr.it

E. Longo, Prof. M. Fanciulli
Dipartimento di Scienze dei Materiali
Università degli Studi di Milano-Bicocca
Via R. Cozzi 55, Milano 20126, Italy

A. Khanas, Dr. A. Zenkevich
Moscow Institute of Physics and Technology
Dolgoprudny, Moscow region 141701, Russia

Prof. M. Cantoni, Dr. C. Rinaldi
Dipartimento di Fisica
Politecnico di Milano
Via G. Colombo 81, Milano 20131, Italy

The ORCID identification number(s) for the author(s) of this article can be found under https://doi.org/10.1002/admi.202000905.

DOI: 10.1002/admi.202000905

Table 1. List of the analyzed samples. The materials stack is the same for all the samples, while the Sb_2Te_3 is subjected to the different indicated RTA, prior to Fe deposition.

		RTA steps on Sb_2Te_3 (prior to Fe deposition)		
Sample	Stack	Ramp up	Heating	Cooling down
SN	^{54}Fe(10 nm)/^{57}Fe(1 nm)/Sb_2Te_3/SiO_2/Si	None	None	None
S150	^{54}Fe(10 nm)/^{57}Fe(1 nm)/Sb_2Te_3/SiO_2/Si	$\overset{10\,s}{\text{RT}} \Rightarrow 150\,^{\circ}C$	$\overset{10\,s}{150\,^{\circ}C} \Rightarrow 150\,^{\circ}C$	$\overset{250\,s}{150\,^{\circ}C} \Rightarrow \text{RT}$
S200	^{54}Fe(10 nm)/^{57}Fe(1 nm)/Sb_2Te_3/SiO_2/Si	$\overset{10\,s}{\text{RT}} \Rightarrow 200\,^{\circ}C$	$\overset{10\,s}{200\,^{\circ}C} \Rightarrow 200\,^{\circ}C$	$\overset{250\,s}{200\,^{\circ}C} \Rightarrow \text{RT}$

to different FM/TI systems, providing a general procedure to improve their interface quality.

2. Experimental Section

The deposition of polycrystalline Sb_2Te_3 thin films was carried out by MOCVD at room temperature (RT) on large-area (4″) SiO_2/Si substrates. Previous analysis by scanning electron microscopy (SEM) evidenced a granular morphology of the deposited layers, and a nominal thickness of about 30 nm.[13] The topological nature of this material was proven through magneto-transport measurements.[7] The samples were subsequently transferred to a chamber equipped with pulsed laser deposition (PLD) for the growth of ^{54}Fe(10 nm)/^{57}Fe(1 nm) bilayers on Sb_2Te_3 at RT, similarly to what was reported in ref. [8]. In particular, the isotopically enriched (95%) 1 nm thick ^{57}Fe interlayer allowed to perform interface-sensitive CEMS to get atomic-scale structural, chemical and magnetic information about the interface.[14–16]

The quality of the Fe/Sb_2Te_3 interface was studied with different RTA in N_2. The first treatment was the same recipe used in ref. [14] to improve the interface sharpness in other Fe/oxide systems. However, this RTA process turned out to be detrimental for its interface quality in the case of Fe/Sb_2Te_3.[8] Alternatively, the annealing was then performed on the Sb_2Te_3 layer only, prior to Fe deposition. While both a rapid or a slow-ramp thermal annealing at 200 °C were tested (Figure S1, Supporting Information), the RTA turned out to be more effective in improving the Sb_2Te_3 crystalline quality.

Table 1 summarizes the stacks with the corresponding RTA treatments of Sb_2Te_3 applied before Fe deposition.

The X-ray based structural-chemical analysis was performed by GIXRD and XRR measurements. GIXRD used the Cu–K_α line ($\lambda = 1.54$ Å) and the diffraction patterns were collected with a position-sensitive gas detector (Inel CPS-120).[17] The rocking angle between the sample and the X-ray beam was fixed at $\omega = 2°$. XRR measurements allowed the determination of the thickness, the roughness and the electronic density (ρ_e) of each layer composing the sample. The XRR data were obtained using a commercial scintillator and modelled through a matrix formalism corrected by a Croce-Nevot factor. In particular, ρ_e is related to the measured critical vector Qc by the relation $Qc(\text{Å}^{-1}) = 0.0375\sqrt{\rho_e(e^{-}\text{Å}^{-3})}$ (for the Cu K_α emission).

Magnetic hysteresis loops were measured by VSM using a MicroSense EZ-9. VSM data provided the value of the saturation magnetization (M_s) and the direction of the easy axis of the magnetization at RT.

The elemental distribution in the heterostructures was determined by ToF-SIMS. An ION TOF IV, using Cs^+ ions with 500 eV for sputtering and Ga^+ ions at E = 25 keV, was used for the analysis. Secondary ions were collected in negative polarity and in interlaced mode. Under such operating conditions, in a Fe (or FeO_x) matrix, the sensitivity of the secondary ion FeO^- is enhanced with respect to the elemental Fe^- ion under Cs^+ sputtering.[18]

CEMS analysis was carried out at RT in a constant-acceleration drive, with the sample mounted as an electrode in a parallel-plate avalanche detector filled with acetone gas. An α-Fe foil at RT was used for the CEMS velocity scale calibration and all the reported isomer shifts were relative to α-Fe.

3. Results and Discussion

3.1. Structural and Magnetic Properties of the Fe/Sb_2Te_3 Heterostructure

Figure 1 shows the XRR analysis of the SN and S200 samples, while **Table 2** reports the parameters obtained by the fit of XRR data (nominal layers' thicknesses, electronic density

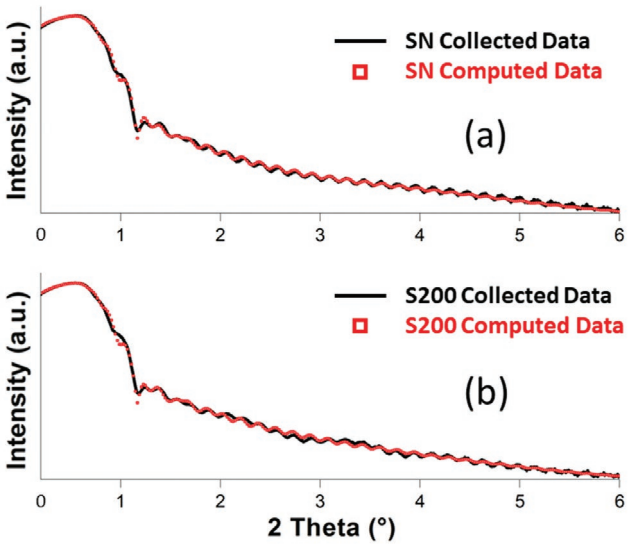

Figure 1. The collected XRR spectra (black solid line) and their computed models (red squares) for samples (a) SN and (b) S200.

Table 2. Values extracted from the fit of the XRR curves of the samples SN and S200. The error on thickness and roughness is ± 0.1 nm and ± 0.05 e^- $Å^{-3}$ on electronic density.

Layers	Thickness [nm]	ρ_e [e^- $Å^{-3}$]	Roughness [nm]
	SN/S200	SN/S200 [nominal]	SN/S200
FeO	2.8/3.1	1.7/1.7 [1.6]	2.4/2.3
Fe	6.2/6.3	2.2/2.2 [2.2]	2.4/2.0
Sb_2Te_3	27.7/27.7	1.5/1.5 [1.6]	2.3/2.1
Sb_2O_3	1.6/1.5	1.4/1.5 [1.5]	0.2/0.1
SiO_2	50.0/50.3	0.8/0.8 [0.8]	0.4/0.4

and surface/interface roughness), modelling the system with five layers. As evident from Table 2, the layers thickness and electronic density are not affected by the annealing, so that the stack is perfectly preserved. A slight decrease of the Sb_2Te_3 (and Fe) surface roughness is detected, which plays a relevant role in determining the Fe/Sb_2Te_3 interface quality, as it will be substantiated later in the manuscript.

On the other hand, the crystal quality of the Fe and Sb_2Te_3 layers was largely affected by the thermal annealing. **Figure 2** shows the GIXRD patterns for all samples (Table 1) and the data are compared to the powder diffraction pattern of cubic α-Fe (black line) and Sb_2Te_3 (pink line). The latter is characterized by a rhombohedral crystal structure belonging to the R-3m space group.[19] In agreement with previous studies,[20] the crystalline grains of the Sb_2Te_3 substrate showed an out-of-plane (OOP) orientation along the [00ℓ] direction. Through X-ray measurements conducted in Bragg–Brentano geometry, we correlated the higher intensity of the (003), (006), and (009) peaks present in the GIXRD patterns, as compared to the powder, with the presence of such [00ℓ] OOP orientation.[8] From Figure 2, we observed that the peaks relative to the [00ℓ] direction acquire intensity and sharpness as a function of the RTA temperature, as highlighted in Figure 2d. This corresponds to an improvement of the Sb_2Te_3 layer crystallization and indicates that the amorphous fraction of the as-deposited Sb_2Te_3 compound becomes crystalline and oriented along the [00ℓ] direction. Moreover, the overall enhancement of the Sb_2Te_3 layer reflects in a higher intensity of the other diffraction peaks, as clear at $2\theta \approx 38°$ in Figure 2a–c.

The improvement of the Sb_2Te_3 crystallinity by RTA, affects the crystalline quality of the Fe layer subsequently deposited on top. Figure 2e depicts the evolution of the peak at $2\theta \approx 44°$, which corresponds to the reflection from Fe (110) planes in the α phase. Interestingly, the full width at half maximum reduces with the annealing (1.50° in SN, 1.30°–1.35° in S150 and S200), while the intensity increases, pointing toward the formation of larger crystalline grains in Fe deposited onto the annealed Sb_2Te_3 layer.

Figure 3 shows the hysteresis loops acquired by VSM at RT for the samples SN (blue curve) and S200 (red curve), with the external magnetic field applied in the film plane. The easy axis of the magnetization lies in the plane (IP) of the Fe layer, while the OOP direction is a hard axis, as evident from the comparison of the red/blue and green lines in the inset of Figure 3. This agrees with CEMS (see the next section), and results from the magnetic shape anisotropy contribution in such thin films.

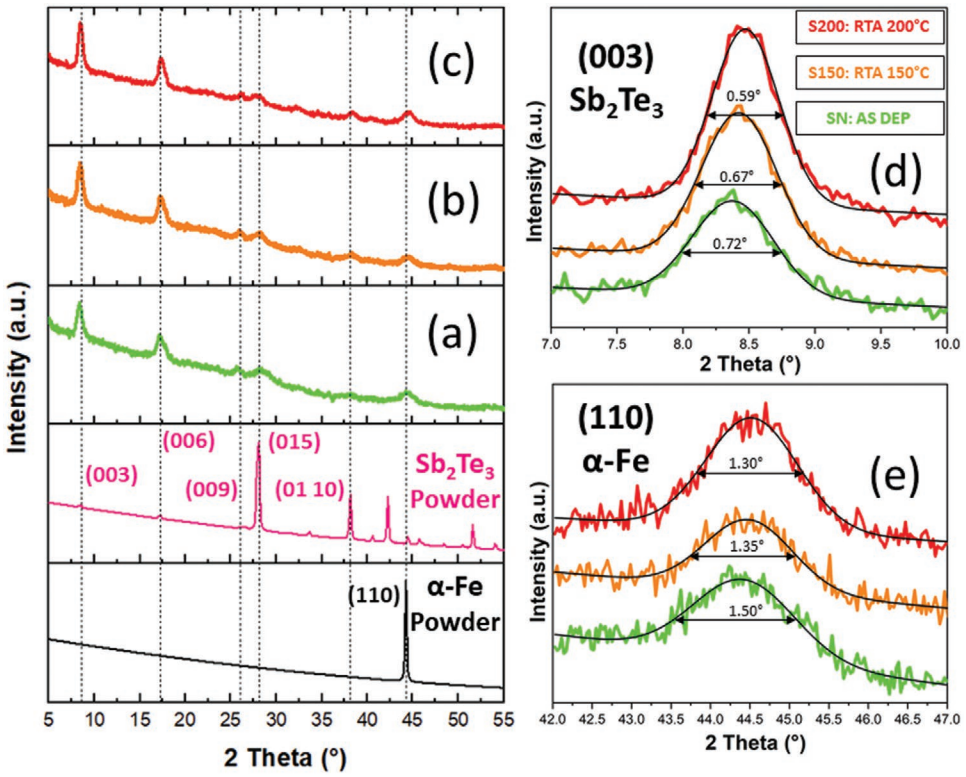

Figure 2. GIXRD pattern of samples (a) SN, (b) S150, and (c) S200. For the Sb_2Te_3 and α-Fe powder diffraction patterns, please refer to ICSD code: 2084 and ICSD code: 53802, respectively. d,e) The evolution of the Sb_2Te_3 (003) and Fe (110) reflections with the thermal annealing, respectively.

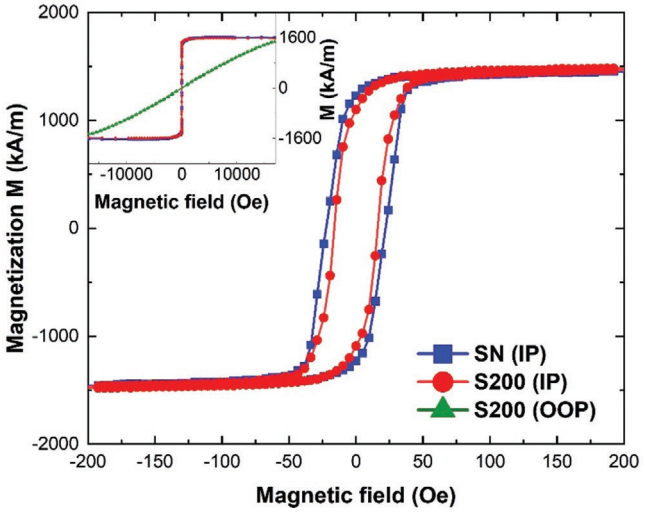

Figure 3. In-plane magnetic hysteresis loops for the samples SN (blue curve) and S200 (red curve) at relatively low fields. The inset shows the magnetic response up to saturation. The green curve shows the out-of-plane loop for sample S200.

M_s is around 1600 kA m^{-1} (or emu cm^{-3}) for the two samples (within the error bar of about 5%). The value of M_s, very similar to that reported for bulk α-Fe (1700 kA m^{-1}), evidenced the good magnetic quality of the films, also considering the presence of a FeO_x layer at the surface (Table 2) due to the absence of any capping layer. The squareness of the hysteresis loops, (i.e., the ratio between the magnetization at remanence and at saturation) was around 70% for both the samples, compatible with the polycrystalline structure of the film. The coercive field reduced from 22 Oe in SN to 16 Oe in S200. We attributed this change to the enhanced crystalline degree of Fe (Figure 2e), which possibly induces the formation of larger grains and magnetic domains of Fe, when deposited on Sb_2Te_3 subjected to RTA. In general, the decrease of the coercive field for a ferromagnetic film in contact with a thermally treated 3D-TI could be beneficial in devices, reducing the energy required to switch the FM magnetization through a spin-transfer torque effect at the FM/TI interface.

3.2. Effect of the Sb_2Te_3 RTA on the Chemical, Structural, and Magnetic Properties of the Fe/Sb_2Te_3 Buried Interface

ToF-SIMS was performed on samples SN and S200 and the result is reported in **Figure 4**. The higher sensitivity for the Fe atoms detection was reached by tracking the ^{54}FeO (orange line) and ^{57}FeO (green line) profiles across the heterostructures, as explained in Section 2. Observing the evolution of the curves, the expected stacking order of the layers is respected. Following the trends versus the sputtering time, it is evident that the ^{54}Fe layer is on top of the stack. After ≈45 s sputtering time, ^{57}Fe shows a relative maximum in both SN and S200 related to the presence of the ^{54}Fe/^{57}Fe interface. The profiles of Te and Sb signals do not show major differences with the annealing. Indeed, Te and Sb intensities quickly drop in FeO_x layer at comparable values in the two samples, suggesting a comparable amount of the element. Further, the slope of the intensity of Te is very similar in both cases, with a marginal reduction for S200, which is associated with the loss of the pile up in intensity at the ^{54}FeO/^{57}FeO interface and possibly related to scarce Te diffusion in the FeO_x layer. Also Sb shows a signal that drops across the interface with nearly the same slope in SN and S200,

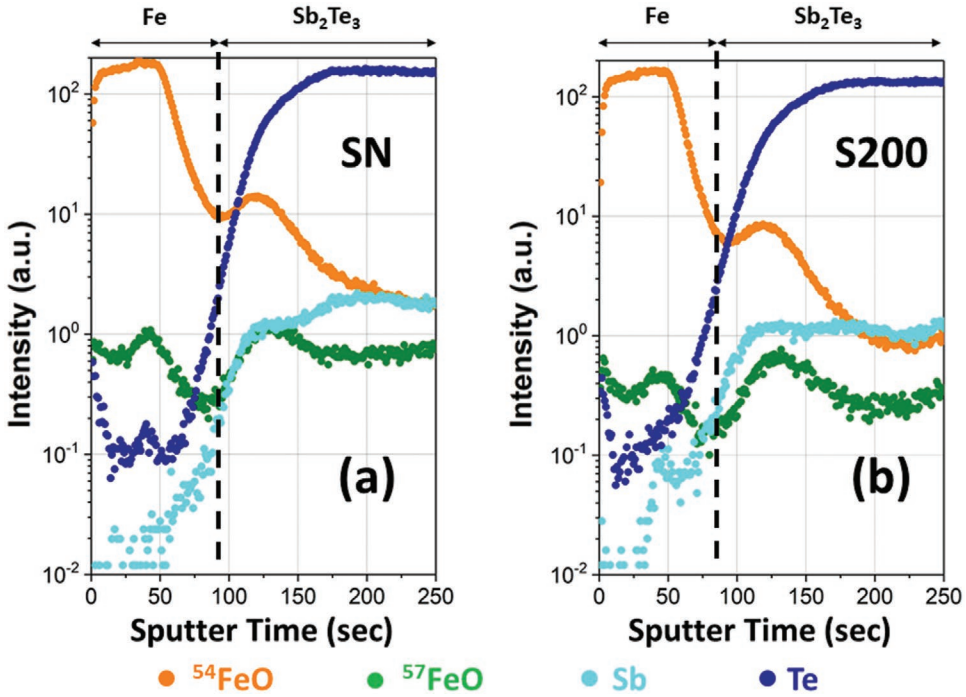

Figure 4. ToF-SIMS measurements of samples (a) SN and (b) S200. A qualitative comparison between (a) and (b) showed that few differences are present in SN and S200, which is a proof of the interface stability following the RTA.

with a possible pile up effect up to the $^{54}FeO/^{57}FeO$ interface. Remarkably, within the technique detection limit, no major Sb diffusion is detected in the Fe layer, pointing toward the absence of intermixing at the interface. As a confirmation, ToF-SIMS analysis demonstrates that the ^{57}Fe tracer-layer is preferentially confined between the ^{54}Fe layer and the Sb_2Te_3 substrate in both SN and S200. The presence of a signal pile up of the ^{57}FeO signal at a sputtering time ≈45 s, corresponding to the beginning of ^{54}FeO drop in intensity following the plateau at shorter sputtering times, strongly suggests the presence of a transition from a matrix rich in ^{54}Fe to a matrix rich in ^{57}Fe. On the contrary, in the case of an ideal intermixing between ^{54}Fe and ^{57}Fe such pile up effect would be lost. Furthermore, moving at longer sputtering times (i.e., toward the substrate), the slope at which the intensity decays is different for ^{54}FeO or ^{57}FeO, confirming the transition to a ^{57}Fe-enriched region, despite the knock of ^{54}Fe due to the sputtering. The decrease of the Fe signal is also related to the change in the intensity of oxygen in the different regions of the samples, which affects the secondary ions yield (note that the oxygen profile is the same for both SN and S200 samples) (Figure S3, Supporting Information). Following such considerations, we attribute the chemical, structural and magnetic characterization by CEMS (described below) exclusively to the buried $^{57}Fe/Sb_2Te_3$ interface.

Figure 5a shows the ^{57}Fe-CEMS analysis on samples SN, S150, and S200. All the spectra could be analyzed in terms of four components: α-Fe, DIST, DOUB-1, and DOUB-2, as in ref. [8]. **Table 3** summarizes the fitting parameters, where δ indicates the isomer shift, ΔE_Q the quadrupole splitting, $\langle B_{hf}\rangle$ the average hyperfine magnetic field, $\langle\Gamma\rangle$ the average line width and A_{25} the ratio between lines (1,6) and (2,5) of the magnetically-split components. Figure 5b shows the evolution of the relative spectral areas for each fitting component, as obtained by assuming the Debye–Waller factor equal to 1 for all of them. The fitting strategy was to fix the value of the hyperfine parameters for all the fitted components in SN, S150, and S200, while the relative areas (Figure 5b) and the $\langle B_{hf}\rangle$ of the DIST component (Table 3) are the free parameters for the fit.

Table 3. CEMS parameters extracted from the fit of the data shown in Figure 5a. Where the experimental error is not indicated, this means the parameter was fixed during the fitting procedure.

	Parameters	α-Fe	DIST	DOUB-1	DOUB-2
	δ (mm s^{-1})	0,0	0,17(1)	0,46(1)	0,64(2)
	ΔE_Q (mm s^{-1})	0,0	0,0	0,52(1)	1,95(3)
SN	$\langle B_{hf}\rangle$(T)	33,02(3)	26,58(3)	–	–
S150	$\langle B_{hf}\rangle$(T)	33,02(3)	28,57(3)	–	–
S200	$\langle B_{hf}\rangle$(T)	33,02(3)	28,82(3)	–	–
	$\langle\Gamma\rangle$ (mm s^{-1})	0.35(1)	0.5	0.5	1,72(4)
	A_{25}	4	4	–	–

The α-Fe contribution is due to ^{57}Fe atoms in an unperturbed local environment. DIST is a distribution of broadened

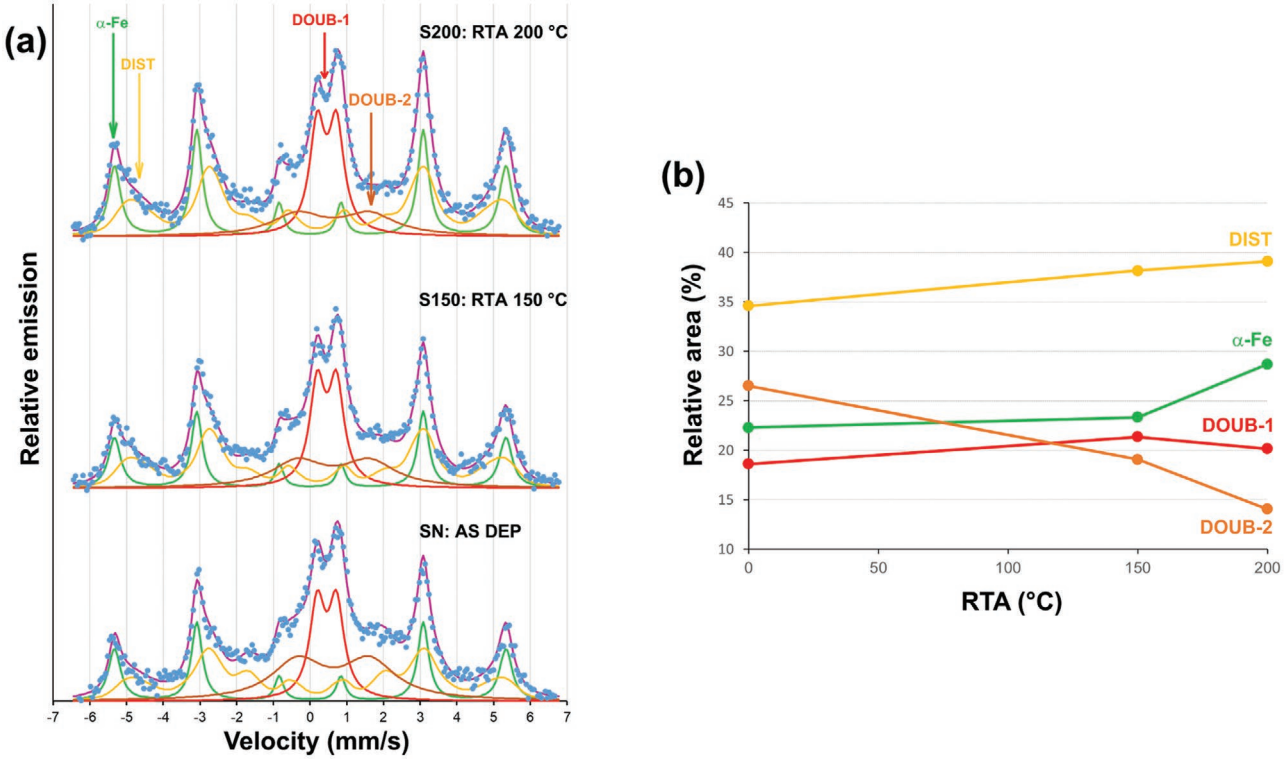

Figure 5. a) CEMS measurements of samples SN, S150, and S200. The blue points are the experimental data and the superimposed purple solid line is the simulated curve, as obtained by the sum of the indicated fitting components: a-Fe, DIST, DOUB-1, and DOUB-2; (b) corresponding RTA-dependence of the relative areas of the four fitting components.

magnetically-split sextets, and it is attributed to undercoordinated ^{57}Fe atoms in direct contact with the Sb_2Te_3 layer. When compared to α-Fe, DIST is characterized by a lower $<B_{hf}>$ and an enhanced δ (Table 3), thus pointing to the occurrence of a hybridization between the Fe atoms and Sb_2Te_3, leading to a lower electronic density around Fe atoms at the interface.[8] The doublets DOUB-1 and DOUB-2 are associated with two paramagnetic phases. DOUB-1 is attributed to FeTe, while DOUB-2 was previously attributed either to the presence of FeO_x or $FeSb_2$.[8] The A_{25} value associated with this ferromagnetic portion showed that the magnetization is always directed in the film plane, in accordance with the VSM data (Figure 3). The increase of $<B_{hf}>$ for the DIST component in S200, when compared to SN (Table 3), further supported the hypothesis that, upon the RTA of Sb_2Te_3, the Fe atoms at the Fe/Sb_2Te_3 interface tend to reorganize toward pure α-Fe. As a matter of fact, we detected an ≈8% increase of the $<B_{hf}>$ for the DIST component when moving from SN to S200 (Table 3). This reflects an overall increase of the magnetic moment at the Fe/Sb_2Te_3 interface, as originated from the higher crystallinity of the corresponding underlying Sb_2Te_3 layer.

Figure 5b summarizes the main effect of the RTA of Sb_2Te_3, on the chemical, structural and magnetic configuration of the Fe atoms at the interface, where a gradual increase of the magnetic (α-Fe + DIST) fraction (of ≈11%) is observed. Correspondingly, a gradual lowering of the DOUB-2 fraction (from ≈27% to ≈14%) is observed (error bars in the spectral areas is around 2%). Based on the present findings, we attribute the DOUB-2 component to FeO_x. The RTA is demonstrated to favor the formation of a sharper and structurally purer Fe/Sb_2Te_3 interface. The presence of O at the Sb_2Te_3 surface is unavoidable, as far as Sb_2Te_3 is exposed to the atmosphere without a proper capping layer prior to the transfer to the PLD system for the deposition of Fe. Here, the result of this work comes: the demonstration of an almost complete restoration of the Sb_2Te_3 crystalline quality and chemical purity by an appropriate mild thermal processing. To a certain extent, the result permits to avoid the capping–decapping procedure in the growth of FM/TI heterostructures.

GIXRD and CEMS data from several samples were compared (Section S2, Supporting Information) to provide an overview on the chemical-structural differences among the samples studied in this work and those previously reported.[8] The differences were mainly attributed to the crystalline quality of the as-deposited Sb_2Te_3. In particular, the SN sample studied in the present work is characterized by a higher crystallinity, which was correlated with the higher fraction of the magnetic DIST component of the CEMS data at the expense of the paramagnetic fraction, when compared to the as-deposited case reported in ref. [8].

Recently, it was shown that proper annealing procedures of Sb_2Te_3 grown on top of Si(111) produce epitaxial TI.[22] Even if epitaxial Sb_2Te_3 is not possible on (amorphous) SiO_2, the enhancement in the Sb_2Te_3 crystallinity detected by GIXRD (Figure 2d) is clear when comparing S200 and SN. It simultaneously determines a lower Sb_2Te_3 surface roughness, which favors a higher crystallinity of Fe (Figure 2e), a lower Fe roughness (Table 2), and a lower intermix in S200 when compared to SN (Figure 5). A similar effect was observed in Fe/oxide heterostructures,[14] further supporting this scenario.

3.3. Formation of FeTe at the Fe/Sb_2Te_3 Interface

The detection of DOUB-1 by CEMS, and its attribution to FeTe is of particular interest. There is a negligible change in the FeTe fraction upon RTA (Figure 5b). This result nicely supports previous insights about a strong tendency of Fe to bond with the chalcogenide atoms of chalcogenide-based TI.[8,9] Moreover, the presented RTA experiments marked an upper limit for the thermal treatment that preserves the FeTe before being affected by the Sb_2Te + 2Te dissociation, as observed for $T > 200$ °C (Figure S1, Supporting Information).

The potential role that this small fraction of interfacial FeTe can play in a charge-to-spin conversion in Fe/Sb_2Te_3 is difficult to foresee, even if in general it could be detrimental. On the other hand, at the particular conditions, the stabilization of the FeTe phase may give rise to superconductivity, and the Fe/FeTe/Sb_2Te_3 system could be of potential interest for investigating the exotic interplay between superconductivity, topology, and magnetism.[21,23,24] For these reasons, in the following, we provide a thermodynamic picture of the formation of FeTe at the Fe/Sb_2Te_3 interface.

Vobornik et al.[11] and Walsh et al.[10] for several FM/TI compounds, reported the favorable stability of FeTe based on thermodynamics arguments. The equation $\Delta G^0 = \Delta H^0 - T\Delta S^0$ is the standard-state Gibbs free energy variation as a function of the changes in the enthalpy H and entropy S in the system ($\Delta G^0(H,S)$), at the absolute temperature T (here fixed at T = 298 K). In ref. [11], the authors have investigated the possible reactions that could take place at the Fe/Bi_2Te_3 interface using a standard thermodynamic tabulation,[25] highlighting the natural tendency of Fe atoms to react with Bi_2Te_3 forming $FeTe_{0.9}$ ($\Delta G^0_{FeTe_{0.9}}$ spans from -4.5 to $0.5\frac{kJ}{mol\cdot Fe}$) and $FeTe_2$ ($\Delta G^0_{FeTe_2}$ spans from -17.5 to $-6.6\frac{kJ}{mol\cdot Fe}$) compounds. Similarly, in ref. [10], the Fe/Bi_2Se_3 was investigated in terms of thermodynamic properties, pointing out, also in this case, the high reactivity between Fe and Se atoms. In particular, the formation of Fe_3Se_4 ($\Delta G^0_{Fe_3Se_4} = -244.0\frac{kJ}{mol\cdot Fe}$) was identified as the most favorable. Through angle-resolved X-ray photoemission spectroscopy on Fe/Bi_2Se_3, they showed the formation of $FeSe_x$. The values of ΔG^0 for the $FeSe_{0.961}$ and $FeSe_2$ formation (not shown in ref. [10]) are calculated and reported in Section S4, Supporting Information.

Here we performed similar thermodynamic calculations for the Fe/Sb_2Te_3 systems. The possible chemical reactions we identified are those indicated in the following equations:

$$3Fe + 0.9Sb_2Te_3 \rightarrow 3FeTe_{0.9} + 1.8Sb \quad \Delta G^0_{FeTe_{0.9}} = -8.09\frac{kJ}{mol\cdot Fe} \quad (1)$$

$$Fe + 0.9Sb_2Te_3 \rightarrow FeTe_{0.9} + 1.8SbTe \quad \Delta G^0_{FeTe_{0.9}} = 100\frac{kJ}{mol\cdot Fe} \quad (2)$$

$$3Fe + 2Sb_2Te_3 \rightarrow 3FeTe_2 + 4\,Sb \quad \Delta G^0_{FeTe_2} = -34.8\frac{kJ}{mol\cdot Fe} \quad (3)$$

$$Fe + 2Sb_2Te_3 \rightarrow FeTe_2 + 4SbTe \quad \Delta G^0_{FeTe_2} = 661.3 \frac{kJ}{mol \cdot Fe} \tag{4}$$

We did not consider other possibilities connected to the dissociation of Sb_2Te_3 in $FeTe_x + Sb_2Te$ since, at least to our knowledge, no thermodynamic data are available for the Sb_2Te binary compound. The most favored reactions between Fe and Sb_2Te_3 involve the formation of $FeTe_{0.9}$ and $FeTe_2$ accompanied by the dissociation of the elemental Sb. On the contrary, the formation of the SbTe compound is highly unfavorable.

Of course, it would be very interesting to develop a theoretical model of the Fe/Sb_2Te_3 interface evolution from a thermodynamic point of view, with a special focus on the thermally induced tuning of the chemical, structural or magnetic properties. We hope our results will further boost the use of first-principles multiscale modeling in this sense.[26]

4. Conclusion

We performed a comprehensive chemical, structural, and magnetic study of the Fe/Sb_2Te_3 heterostructure as a function of the RTA of the Sb_2Te_3 layer up to 200 °C, prior to Fe deposition. The combination of XRR, GIXRD, VSM, ToF-SIMS, and CEMS analyses demonstrated a clear correlation between the crystalline quality enhancement of the Sb_2Te_3 layer and the improvement in the chemical, structural, and magnetic properties of the buried Fe/Sb_2Te_3 interface, which also partly affected the macroscopic magnetic properties of the 10 nm-Fe layer. The Fe/Sb_2Te_3 interface is chemically stable up to 200 °C, and the overall stack is preserved. Interface-sensitive CEMS analysis shows an increase of about 11% of the overall magnetic fraction in the case of the annealed substrate, with a lowering of the FeO_x paramagnetic fraction at the interface. Interestingly, the ≈20% fraction of FeTe at the interface was almost unaffected by the RTA, thus strongly suggesting that thermodynamics favors the formation of such a compound at the interface even at RT. We suggest that the tendency of Fe to bond with the chalcogenide atom of a chalcogenide-based TI to be a general phenomenon, as also supported by data available in literature.

In principle, the proposed RTA process can be extended to other FM/TI systems, thus providing a tool for optimizing the interface quality without the use of TI capping interlayers. At the same time, the conducted atomic-scale analysis of the interface properties, revealed the importance of controlling the chemical reactions taking place at the Fe/TI interface during the Fe deposition, especially for monitoring the formation of paramagnetic compounds, potentially detrimental for charge-to-spin conversions applications.

Moreover, the appropriate engineering of ultrathin FeTe-based superconductors in the $Fe/FeTe/Sb_2Te_3$ heterostructures may open strategies to exploit the interplay between topology and superconductivity to investigate on the elusive Majorana fermion, as previously proposed.[21]

Supporting Information

Supporting Information is available from the Wiley Online Library or from the author.

Acknowledgements

The authors acknowledge the Horizon 2020 project SKYTOP "Skyrmion-Topological Insulator and Weyl Semimetal Technology" (FETPROACT-2018-01, No. 824123). C.R. acknowledges the project ECOS by Fondazione Cariplo and Regione Lombardia, Grant No. 2017-1622, and the PRIN project TWEET funded by MIUR (No. 2017YCTB59). A.Z. acknowledges support from the Ministry of Science and Higher Education of the Russian Federation (agreement No. 075-00337-20-03, project FSMG-2020-0001). This article was amended on October 9, 2020 to correct the y-axis of Figure 5(a).

Conflict of Interest

The authors declare no conflict of interest.

Keywords

ferromagnetism, spintronics, topological insulators

Received: May 22, 2020
Revised: July 1, 2020
Published online: August 23, 2020

[1] J. Sinova, S. O. Valenzuela, J. Wunderlich, C. H. Back, T. Jungwirth, *Rev. Mod. Phys.* **2015**, *87*, 1213.
[2] F. Hellman, A. Hoffmann, Y. Tserkovnyak, G. S. D. Beach, E. E. Fullerton, C. Leighton, A. H. MacDonald, D. C. Ralph, D. A. Arena, H. A. Dürr, P. Fischer, J. Grollier, J. P. Heremans, T. Jungwirth, A. V. Kimel, B. Koopmans, I. N. Krivorotov, S. J. May, A. K. Petford-Long, J. M. Rondinelli, N. Samarth, I. K. Schuller, A. N. Slavin, M. D. Stiles, O. Tchernyshyov, A. Thiaville, B. L. Zink, *Rev. Mod. Phys.* **2017**, *89*, 025006.
[3] A. Soumyanarayanan, N. Reyren, A. Fert, C. Panagopoulos, *Nature* **2016**, *539*, 509.
[4] Y. Wang, D. Zhu, Y. Wu, Y. Yang, J. Yu, R. Ramaswamy, R. Mishra, S. Shi, M. Elyasi, K.-L. Teo, Y. Wu, H. Yang, *Nat. Commun.* **2017**, *8*, 1364.
[5] Y. Wang, R. Ramaswamy, H. Yang, *J. Phys. D: Appl. Phys.* **2018**, *51*, 273002.
[6] A. R. Mellnik, J. S. Lee, A. Richardella, J. L. Grab, P. J. Mintun, M. H. Fischer, A. Vaezi, A. Manchon, E.-A. Kim, N. Samarth, D. C. Ralph, *Nature* **2014**, *511*, 449.
[7] R. Cecchini, R. Mantovan, C. Wiemer, L. Nasi, L. Lazzarini, M. Longo, *Phys. Status Solidi RRL* **2018**, *12*, 1800155.
[8] E. Longo, C. Wiemer, R. Cecchini, M. Longo, A. Lamperti, A. Khanas, A. Zenkevich, M. Fanciulli, R. Mantovan, *J. Magn. Magn. Mater.* **2019**, *474*, 632.
[9] S. Majumder, K. Jarvis, S. K. Banerjee, K. L. Kavanagh, *J. Vac. Sci. Technol., B: Nanotechnol. Microelectron.: Mater., Process., Meas., Phenom.* **2017**, *35*, 04F105.
[10] L. A. Walsh, C. M. Smyth, A. T. Barton, Q. Wang, Z. Che, R. Yue, J. Kim, M. J. Kim, R. M. Wallace, C. L. Hinkle, *J. Phys. Chem. C* **2017**, *121*, 23551.
[11] I. Vobornik, G. Panaccione, J. Fujii, Z.-H. Zhu, F. Offi, B. R. Salles, F. Borgatti, P. Torelli, J. P. Rueff, D. Ceolin, A. Artioli, M. Unnikrishnan, G. Levy, M. Marangolo, M. Eddrief, D. Krizmancic, H. Ji, A. Damascelli, G. van der Laan, R. G. Egdell, R. J. Cava, *J. Phys. Chem. C* **2014**, *118*, 12333.
[12] C. Rinaldi, S. Varotto, M. Asa, J. Sławińska, J. Fujii, G. Vinai, S. Cecchi, D. Di Sante, R. Calarco, I. Vobornik, G. Panaccione, S. Picozzi, R. Bertacco, *Nano Lett.* **2018**, *18*, 2751.

[13] M. Longo, S. Cecchi, S. Selmo, M. Fanciulli, C. Wiemer, J.-L. Battaglia, A. Saci, A. Kusiak, in *2015 1st Workshop on Nanotechnology in Instrumentation and Measurement (NANOFIM)*, IEEE, Piscataway, NJ, **2015**, pp. 150–154.
[14] R. Mantovan, C. Wiemer, A. Lamperti, M. Georgieva, M. Fanciulli, A. Goikhman, N. Barantsev, Y.u. Lebedinskii, A. Zenkevich, *Hyperfine Interact.* **2009**, *191*, 41.
[15] A. Zenkevich, R. Mantovan, M. Fanciulli, M. Minnekaev, Y.u. Matveyev, Y.u. Lebedinskii, S. Thiess, W. Drube, *Appl. Phys. Lett.* **2011**, *99*, 182905.
[16] R. Mantovan, C. Wiemer, A. Zenkevich, M. Fanciulli, in *ICAME 2005* (Eds: P. E. Lippens, J. C. Jumas, J. M. R. Génin), Springer, Berlin **2007**.
[17] C. Wiemer, S. Ferrari, M. Fanciulli, G. Pavia, L. Lutterotti, *Thin Solid Films* **2004**, *450*, 134.
[18] S. Suzuki, K. Yanagihara, S. Hayashi, T. Mori, *J. Surf. Anal.* **1999**, *5*, 278.
[19] H. Zhang, C.-X. Liu, X.-L. Qi, X. Dai, Z. Fang, S.-C. Zhang, *Nat. Phys.* **2009**, *5*, 438.
[20] E. Longo, R. Mantovan, R. Cecchini, M. D. Overbeek, M. Longo, G. Trevisi, L. Lazzarini, G. Tallarida, M. Fanciulli, C. H. Winter, C. Wiemer, *Nano Res.* **2020**, *13*, 570.
[21] Y. Mizuguchi, F. Tomioka, S. Tsuda, T. Yamaguchi, Y. Takano, *Phys. C* **2009**, *469*, 1027.
[22] M. Rimoldi, R. Cecchini, C. Wiemer, A. Lamperti, E. Longo, L. Nasi, L. Lazzarini, R. Mantovan, M. Longo, *RSC Adv.* **2020**, *10*, 19936.
[23] S. Manna, A. Kamlapure, L. Cornils, T. Hänke, E. M. J. Hedegaard, M. Bremholm, B. B. Iversen, P.h. Hofmann, J. Wiebe, R. Wiesendanger, *Nat. Commun.* **2017**, *8*, 14074.
[24] Q. L. He, H. Liu, M. He, Y. H. Lai, H. He, G. Wang, K. T. Law, R. Lortz, J. Wang, I. K. Sou, *Nat. Commun.* **2014**, *5*, 4247.
[25] M. Binneweis, E Milke, *Thermochemical Data of Elements and Compounds*, Wiley-VCH, Weinheim, Germany **2002**, pp. i–iv.
[26] B. Mortazavi, E. V. Podryabinkin, S. Roche, T. Rabczuk, X. Zhuang, A. V. Shapeev, *Mater. Horiz.* **2020**, https://pubs.rsc.org/en/content/articlelanding/2020/MH/D0MH00787K.